

Research Article

Single-particle Mineralogy of Asbestos Mineral Particles by the Combined Use of Low-Z Particle EPMA and ATR-FTIR Imaging Techniques

Muhammad Saiful Islam Khan^{1),2)}, Hanjin Yoo^{1),3)}, Li Wu⁴⁾, Hayeong Lee¹⁾, Minjeong Kim¹⁾, Jonghyeon Park¹⁾, Chul-Un Ro^{1),3),*}

¹⁾Department of Chemistry, Inha University, Incheon 22212, Republic of Korea

²⁾School of Medicine, Akfa University, Tashkent, Uzbekistan

³⁾Particle Pollution Management Center, Inha University, Incheon 21999, Republic of Korea

⁴⁾School of Earth Science System, Tianjin University, Tianjin, China

***Corresponding author.**

Tel: +82-32-860-7676

E-mail: curo@inha.ac.kr

Received: 13 November 2022

Revised: 24 November 2022

Accepted: 24 November 2022

ABSTRACT In this work, two single particle analytical techniques such as a quantitative energy-dispersive electron probe X-ray microanalysis (ED-EPMA), called low-Z particle EPMA, and attenuated total reflectance Fourier transform-Infrared (ATR-FTIR) imaging were applied in combination for the characterization and distinction of six standard asbestos and one non-asbestos Mg-silicate minerals of micrometer size. Asbestos fibers have been reported as a natural carcinogen which causes some serious illness like mesothelioma, asbestosis, and lung cancer. Atmospheric aerosols are heterogeneous mixtures and airborne asbestos fibers would be present due to their extensive industrial uses for various purposes. The fibers could also be airborne from natural and anthropogenic sources. As different asbestos fibers have different carcinogenic properties, it is important to determine different types of individual asbestos and non-asbestos Mg-silicate mineral particles and their sources for the public health management. In our previous works, the speciation of individual aerosol particles was performed by the combined use of the two single-particle analytical techniques, which demonstrated that the combined use of the two analytical techniques is powerful for detailed characterization of externally heterogeneous aerosol particle samples and has great potential for characterization of atmospheric aerosols. In this work, it is demonstrated that the identification and differentiation of asbestiform and non-asbestiform Mg-silicate mineral particles is clearly performed using the two single particle analytical techniques in combination than using either technique individually. Especially, anthophyllite and talc can be differentiated using this analytical approach, which has not been easy up until now.

KEY WORDS Single-particle mineralogy, Asbestos, Talc, Low-Z particle EPMA, ATR-FTIR imaging

1. INTRODUCTION

Asbestos is a generic term representing some naturally occurring fibrous Mg-silicate minerals. Asbestiform minerals belong to two basic mineral groups, i.e., serpentines and amphiboles. Chrysotile is in the serpentine group, while the other five asbestiform minerals, such as actinolite, anthophyllite, amosite, crocidolite, and

tremolite, belong to the amphibole group. The general formulas of the two mineral groups and the idealized formulas of six asbestos minerals and non-asbestiform talc mineral are listed in the second and fourth columns of Table 1, respectively. Silicate tetrahedra are basic building blocks of asbestos fibers; in chrysotile and amphiboles, it may occur as sheet (Si₄O₁₀)⁴⁻ and double chain (Si₄O₁₁)⁶⁻ forms, respectively (Skinner *et al.*, 1988). Amphibole minerals have some structural variations with minor substituents such as Na⁺, K⁺, Fe²⁺, or Fe³⁺ by exchanging cations present between the silicate layers.

Asbestos fibers with special and resilient physical properties (Bernarde, 1990) have been extensively used in cement products, roof coatings, brake pads and shoes, clutches, etc. (Dodson and Hammer, 2011). Most asbestos fiber-containing products used in industrial applications are usually stacked on or physically bound to organic or inorganic supporting materials, so that those fibrous particles are not released into the atmosphere under normal operating conditions. Nevertheless, fibers can be released into the atmosphere from supporting materials or become airborne in various ways such as during manipulation, exclusion, vibration, abrasion, and machining operations (Michaels and Chissick, 1981). The highly resilient physical properties of the asbestos fibers are also likely to make them persist longer in the air. The close relationship between workplace exposure to airborne asbestos fibers and respiratory diseases was

well established in early 1960s (Selikoff *et al.*, 1964), and general concerns for human health due to airborne asbestos led to strict regulations on the asbestos use (Murray, 1990). Airborne asbestos toxicity is one of the most extensively studied topics in modern epidemiology (Bignon *et al.*, 1989; WHO, 1986). Since then, extensive research has been performed to correlate the physicochemical characteristics of airborne asbestos fibers, such as their size, shape, crystal structure, and chemical compositions, with their respective impact on environment and human health. Airborne asbestos fibers may be in a range of size, and yet the aspect ratio of the regulated asbestos fibers (length to width) is at least 5 : 1 (Dodson and Hammer, 2011). It was reported that the upper respirable size limits are smaller than 10 μm and 3 μm for the rounded and fibrous particulates, respectively (Lee and Abraham, 1985). Shorter fibrous particulates of smaller diameter are more likely to enter respiratory tracts, get embedded in lung tissues, and lead to serious health problems like asbestosis, mesothelioma, and lung cancer (Goodhead and Martindale, 1969; Wright, 1969; Knox *et al.*, 1968; Crable, 1966; Newhouse and Thomson, 1965). On the other hand, it was also reported that the different asbestos fibers showed different degrees of carcinogenicity. For example, amphibole fibers such as crocidolite and amosite were reported to be 100 and 500 times more powerful in causing mesothelioma than chrysotile fibers, respectively (Sporn and Roggli, 2004; Gardner and Powell, 1986).

Table 1. Chemical formulas of six asbestiform and one non-asbestiform minerals.

Asbestiform minerals			
Type	General formula	Commercial/mineral name	Idealized chemical formula
Serpentine	(Mg _{3-x} R _x ²⁺ Ry ³⁺)(Si _{2-γ} Ry ³⁺)O ₅ (OH) ₄	Chrysotile (white asbestos)	Mg ₃ (Si ₂ O ₅)(OH) ₄
		Amosite (fibrous grunerite)	(Fe ²⁺) ₂ (Fe ²⁺ ,Mg) ₅ Si ₈ O ₂₂ (OH) ₂
		Actinolite	Ca ₂ (Mg,Fe ²⁺) ₅ Si ₈ O ₂₂ (OH) ₂
Amphibole	A ₀₋₁ B ₂ C ₅ T ₈ O ₂₂ (OH,F,Cl,O) ₂	Anthophyllite	(Mg,Fe) ₇ Si ₈ O ₂₂ (OH) ₂
		Crocidolite (blue asbestos, fibrous riebeckite)	Na(Mg,Fe ²⁺) ₃ (Fe ³⁺) ₂ Si ₈ O ₂₂ (OH) ₂
		Tremolite	Ca ₂ Mg ₅ Si ₈ O ₂₂ (OH) ₂
Non-asbestiform mineral			
	Talc	-	Mg ₃ (Si ₄ O ₁₀)(OH) ₂

R_x²⁺ ≡ Fe²⁺, Mn²⁺/Ni²⁺ and R_y³⁺ ≡ Al³⁺/Fe³⁺
 A ≡ Na⁺/K⁺; B ≡ Mg²⁺, Fe²⁺, Mn²⁺, Ca²⁺, Na⁺/Li⁺;
 C ≡ Mg²⁺, Fe²⁺, Mn²⁺, Al³⁺, Fe³⁺, Cr³⁺/Ti⁴⁺; T ≡ Si⁴⁺/Al³⁺

Hence, it is imperative to effectively differentiate the different forms of asbestos mineral particles, especially in the respirable particulate size range.

Up until now, various analytical techniques have been used to characterize asbestos minerals in diverse environments or matrices such as air, water, soil, building materials, surface dust, lung tissue, etc., which involves the characterization of bulk and single particles or both (Dodson *et al.*, 2008; Dodson and Atkinson, 2006; Millette, 2006; Rohl and Langer, 1974; Rickards, 1972). Bulk asbestos fibers can be characterized by X-ray fluorescence (XRF), X-ray photoelectron spectroscopy (XPS), and X-ray diffraction (XRD), which can provide information on elemental compositions, chemical species, and crystal structures, respectively (Keane and Wallace, 1995). Polarized light microscopy (PLM) technique has been used for identification of bulk asbestos on the basis of their morphology, refractive index, pleochroism, birefringence, and orientation. FT-IR technique has also been used to characterize asbestos fibers based on the characteristic silicate vibrational bands (900–1,200 cm^{-1}) (Hodgson, 1986). Differential thermal analysis (DTA) and thermal gravimetric analysis (TGA) have been used to identify some specific asbestos fibers like chrysotile (Hodgson, 1986). However, these bulk techniques may fail to identify individual particles of asbestos minerals in the presence of other minerals or if fibers are embedded in a matrix (Rohl and Langer, 1974). Various microscopic techniques, such as phase contrast microscopy (PCM), transmission electron microscopy (TEM), scanning electron microscopy (SEM), etc., have been used for characterization of asbestos fibers or individual mineral particles purely based on their morphology. PCM can determine the number concentrations of fibers in the air based on their morphology but cannot differentiate between asbestos and non-asbestos fibers. SEM and high-resolution TEM have been used to identify quite small fibers for the extremely small amount of samples with appropriate peripheral instrumentation (Dodson *et al.*, 2008). However, for positive identification of asbestos fibers or airborne asbestos particulates, the characteristic morphology, chemical composition, and crystal structure are required to be analyzed at the same time. SEM and TEM combined with energy dispersive X-ray spectroscopy (SEM-EDX and TEM-EDX) can provide information on morphology as well as elemental composition of individual mineral particles. The crystal structure can be further obtained when selected area electron

diffraction (SAED) is utilized with TEM-EDX (Janik and Wrona, 2019). This combination of TEM-EDX with SAED, although effective in the positive identification of submicron asbestos particles, is an expensive technique and requires sample pre-treatment with considerable expertise for the operation.

A quantitative energy-dispersive electron probe X-ray microanalysis (ED-EPMA, called low-Z particle EPMA) has been successfully employed in our previous works to quantitatively distinguish between K-feldspar and Na-feldspar particles generated from NIST SRMs (standard Reference Materials) (Khan *et al.*, 2008). Hence, we were encouraged to apply this technique to analyze chemical compositions of individual particles of six standard asbestos minerals as well as talc (a non-asbestos Mg-silicate mineral). On the other hand, although the low-Z particle EPMA technique can provide information on the morphology and elemental concentrations, it is somewhat difficult to clearly differentiate individual Mg-silicate mineral particles with similar stoichiometry but with different crystal structures, such as anthophyllite and talc. On the other hand, the combined use of the low-Z particle EPMA and attenuated total reflectance Fourier transform-infrared (ATR-FTIR) imaging technique for the same individual particle analysis would be powerful to clearly identify the asbestos and non-asbestos minerals on a single particle basis as the two techniques can provide information on morphology, elemental concentrations, and crystal structures of individual aerosol particles (Malek *et al.*, 2019, 2011; Jung *et al.*, 2014, 2010; Song *et al.*, 2013).

In this work, it was demonstrated that the feasibility of the combined use of two standalone single particle analytical techniques, i.e., low-Z particle EPMA and ATR-FTIR imaging, for the identification of and the clear distinction among individual particles of six asbestos and one non-asbestos Mg-silicate mineral particles. Standard asbestos fibers and talc (a non-asbestos Mg-silicate mineral) were ground to micrometer size for single-particle analysis. The complementary information on chemical composition from low-Z particle EPMA and crystal structure from ATR-FTIR imaging technique was obtained for the same individual particles. To the best of the authors' knowledge, this combined approach was applied for the first time to characterize and distinguish individual asbestos and non-asbestos Mg-silicate mineral particles.

2. EXPERIMENTAL SECTIONS

2.1 Samples

Six standard asbestos mineral samples, such as chrysotile, amosite, actinolite, anthophyllite, crocidolite, and tremolite (Health and Safety Laboratory, HSE, Harpur Hill, Buxton, Derbyshire, UK) and talc (a non-asbestos Mg-silicate mineral, Sigma-Aldrich) were selected for analysis. The bulk fibrous minerals were ground to smaller particulate sizes using a mortar and pestle. The ground particles were sieved ($< 20 \mu\text{m}$) and collected on Ag foils in a well dispersed manner suitable for single particle analysis.

2.2 Low-Z Particle EPMA

The low-Z particle EPMA was applied to obtain the information on morphology and elemental compositions of individual mineral particles. The EPMA measurements were carried out using a Jeol JSM-6390 SEM equipped with an Oxford Link SATW ultrathin window EDX detector. The resolution of EDX detector is 133 eV for Mn-K α X-rays. X-ray spectra were recorded under the control of Oxford INCA Energy software. To achieve optimal experimental conditions, such as a low background level in the spectra and high sensitivity for low-Z element analysis, an accelerating voltage of 10 kV was used. The beam current was 1.0 nA for all measurements. More details of the measurement conditions can be found elsewhere (Ro *et al.*, 1999). The net X-ray intensities of the elements were obtained by nonlinear least-squares fitting of the collected spectra using the AXIL program (Vekemans *et al.*, 1994). The elemental concentrations of individual particles were determined from their X-ray intensities by the application of a Monte Carlo calculation combined with reverse successive approximations. (Ro *et al.*, 2003). The quantification procedure provided results accurate within 12% relative deviations between the calculated and nominal elemental concentrations when the method was applied to various types of standard salt or mineral particles (Ro *et al.*, 2001, 2000).

2.3 Principal Component Analysis (PCA)

Principal component analysis (PCA) was performed, using a code built on MATLAB (version 7.11.0) platform (Jolliffe and Cadima, 2016; Jackson, 1991), on chemical composition results obtained for individual particles using low-Z particle EPMA to investigate whether the quantitative compositional results were sufficient to

distinguish between the six asbestos mineral particles and the talc particles.

2.4 ATR-FTIR Imaging Technique

ATR-FT-IR imaging measurements of individual particles were performed using a Perkin-Elmer Spectrum 100 FT-IR spectrometer interfaced to a Spectrum Spotlight 400 FT-IR microscope. For ATR imaging, an ATR accessory employing a germanium hemispherical internal reflection element (IRE) crystal with a diameter of 600 μm was used. The ATR accessory is mounted on the X-Y stage of the FT-IR microscope, and the IRE crystal makes contact with the sample via a force lever. The IRE crystal is scanned laterally by an IR beam, and both the crystal and attached sample are moved under the beam as the X-Y stage is driven by a stepper-motor. Given that the crystal and the sample move together as they are scanned, the initial contact between the crystal and the sample is maintained during the imaging data acquisition. The maximum scan area is limited to $400 \times 400 \mu\text{m}^2$. The ultimate spatial resolution of the IR imaging is approximately equal to the wavelength of the incident IR radiation. However, the hemispherical IRE crystal is similar to a lens, in that the IR beam is condensed when the beam strikes the IRE. The extent of the condensation is proportional to the refractive index of the IRE material (4.0 for germanium) (Griffith and Haseth, 2007). Thus, a spatial resolution of 3.1 μm at $1,726 \text{ cm}^{-1}$ is achieved beyond the ultimate spatial resolution limit (Crane *et al.*, 2007; Van Dalen *et al.*, 2007). A 16×1 pixel mercury cadmium telluride (MCT) array detector was used to obtain FT-IR images with a pixel size of 1.56 μm . For each pixel, an ATR-FTIR spectrum, ranging from 720 to $4,000 \text{ cm}^{-1}$ with a spectral resolution of 4 cm^{-1} , was obtained from four interferograms that were co-added and Fourier-transformed. The position of the crystal on the sample was determined using a visible light optical microscope equipped with a light-emitting diode and a charge-coupled device camera. Additionally, the optical image was used to relocate single particles that had been analyzed using low-Z particle EPMA before the ATR-FTIR imaging measurement, as the optical microscopy provides the image of sufficient spatial resolution. Spectral data processing was performed using the Perkin-Elmer Spectrum IMAGE software. ATR-FTIR spectra for the bulk mineral fiber samples were also obtained using a universal ATR accessory of the Perkin-Elmer Spectrum 100 FT-IR spectrometer, where a diamond

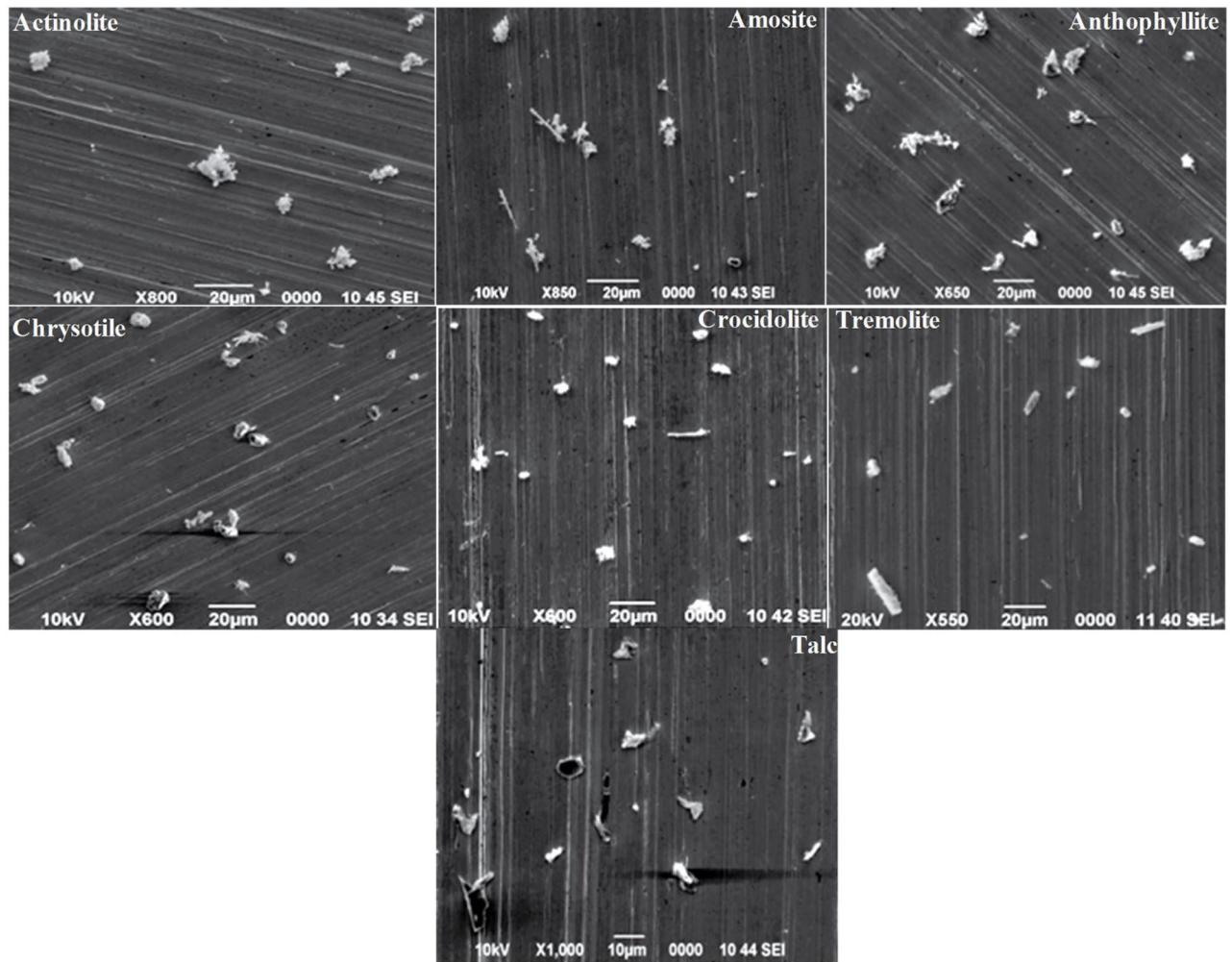


Fig. 1. Typical SE images of six asbestos (actinolite, amosite, anthophyllite, chrysotile, crocidolite, and tremolite) and a non-asbestos (talc) Mg-silicate mineral particles.

was used as the IRE crystal.

3. RESULTS AND DISCUSSION

3.1 Low-Z Particle EPMA

A quantitative single particle analytical technique, low-Z particle EPMA, was employed to examine six asbestiform and one non-asbestiform talc mineral samples. Fig. 1 shows SE image of those particles, where particles of the different samples do not show unique morphology depending on their types (except some rod-like particles of tremolite), indicating the micrometer size particles cannot be identified nor distinguished only from their morphology (Langer *et al.*, 1972). Fig. 2 shows X-ray

spectra and elemental concentrations of typical single particles of the six asbestos and talc minerals together with relative elemental concentrations of Mg, Ca, Fe, Na, and Al normalized to Si. The X-ray spectra of the minerals show that Si and Mg are present in all the mineral types with different relative atomic concentrations. Furthermore, minor Na, Ca, and/or Fe in some mineral types are present characteristically among the mineral types, which seems to be useful to distinguish between the different asbestos and talc minerals. The relative elemental concentrations normalized to Si obtained from the measured single particles for the mineral types are plotted in the right panel of Fig. 2. The relative elemental concentrations for all the mineral types determined by low-Z particle EPMA quite well match with their idealized chemical composi-

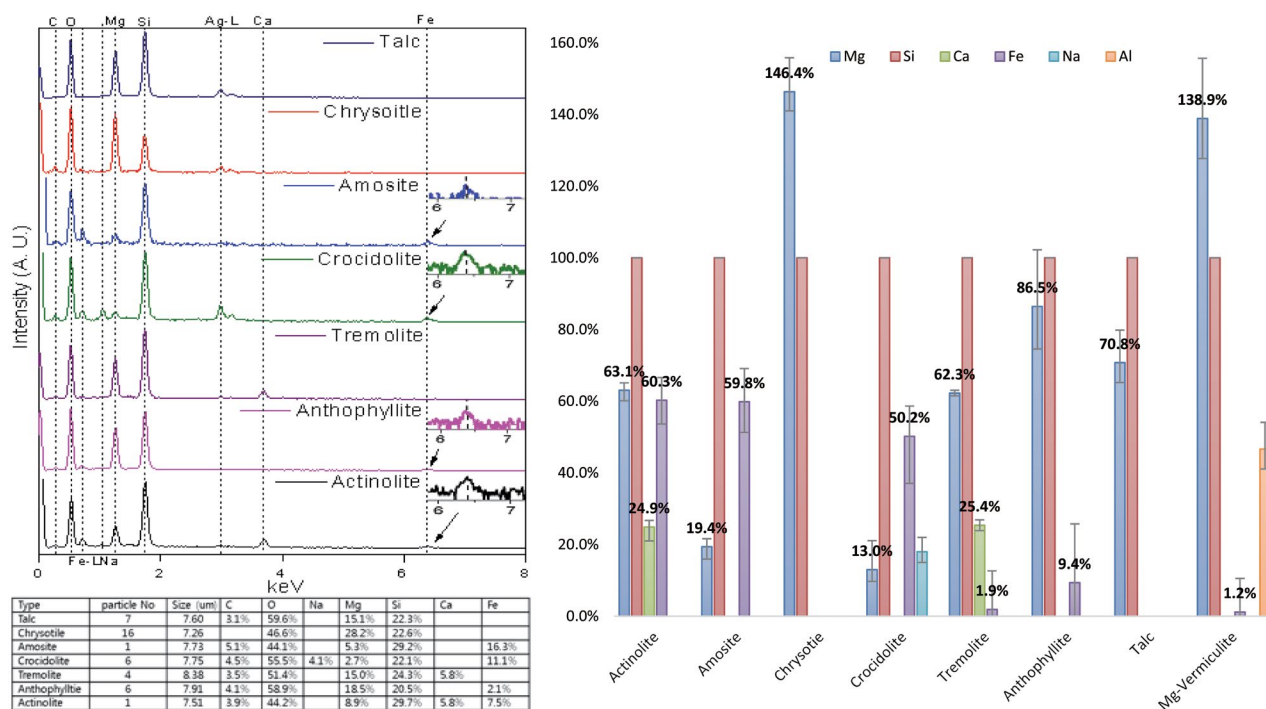


Fig. 2. X-ray spectra and elemental concentrations of six asbestiform and talc minerals on single particle basis and relative elemental concentrations normalized to Si obtained from all the measured single particles for each mineral type (error bars: Min-Max).

tions. Just for an example, the relative atomic concentration of Mg normalized to Si for anthophyllite is 86.5%, which corresponds well to its stoichiometric value of 87.5% (its idealized formula is $(Mg,Fe)_7Si_8O_{22}(OH)_2$). The error bars in the panel are the min-max ranges which indicate the range of the relative elemental concentrations obtained from all the measured single particles for each mineral type. As shown in the right panel of Fig. 2, actinolite ($Ca_2(Mg,Fe^{2+})_5Si_8O_{22}(OH)_2$) can be easily distinguished from the other mineral types as its abundant contents of Mg, Ca, and Fe are unique among the mineral types of interest. Amosite and crocidolite ($(Fe^{2+})_2(Fe^{2+},Mg)_5Si_8O_{22}(OH)_2$ and $Na(Mg,Fe^{2+})_3(Fe^{3+})_2Si_8O_{22}(OH)_2$) are also distinguishable from the others as Mg and Fe are significant with higher Fe than Mg. Amosite and crocidolite are different because of the significant presence and absence of Na in crocidolite and amosite, respectively. Chrysotile ($Mg_3(Si_2O_5)(OH)_4$) is unique among all the mineral types of interest as it is $Mg/Si = 1.46$. Tremolite ($Ca_2Mg_5Si_8O_{22}(OH)_2$) and actinolite ($Ca_2(Mg,Fe^{2+})_5Si_8O_{22}(OH)_2$) are characteristic because of their significant Ca content, but tremolite is distinguishable from actinolite as tremolite has negligible Fe content compared to actinolite. Anthophyllite ($(Mg,Fe)_7$

$Si_8O_{22}(OH)_2$) can be unique as it has a comparably high Mg content to Si with considerable Fe. The non-asbestiform talc mineral ($Mg_3(Si_4O_{10})(OH)_2$) can be also unique as it has a comparably high Mg content to Si without Fe. Based on the low-Z particle EPMA results, the asbestiform and non-asbestiform minerals seem to be well differentiated from each other on a single particle level.

In order to visually examine the low-Z particle EPMA results regarding chemical composition characteristics of the minerals of interest, a multivariate modeling and analysis technique, i.e., principal component analysis (PCA), was performed for the low-Z particle EPMA X-ray data using a MATLAB program. Fig. 3 shows a cluster principal component (PC) scatter plot of the EPMA data for the total seven different groups of individual Mg-silicate minerals on the first two PC axes. The scatter plot shows that amosite, actinolite, crocidolite, and chrysotile minerals are clearly differentiated from the others. On the other hand, anthophyllite, tremolite, and talc belong to one group which cannot be differentiated among themselves on the PC scatter plot, which is strange as the raw EPMA data seem to be quite different between anthophyllite, tremolite, and talc. As the Ca content of tremolite is significant to be differentiated from anthophyllite and talc

based on their EPMA X-ray data, somehow PCA did not take account of the Ca content when the EPMA X-ray data for all the minerals were processed. When PCA analysis was performed using only three data sets of anthophyllite, tremolite, and talc minerals, tremolite was clearly differentiated from anthophyllite and talc, but anthophyllite and talc were not yet separated well on the PC plot (not shown here), indicating that the low-Z particle EPMA can clearly distinguish between all the individual asbestos

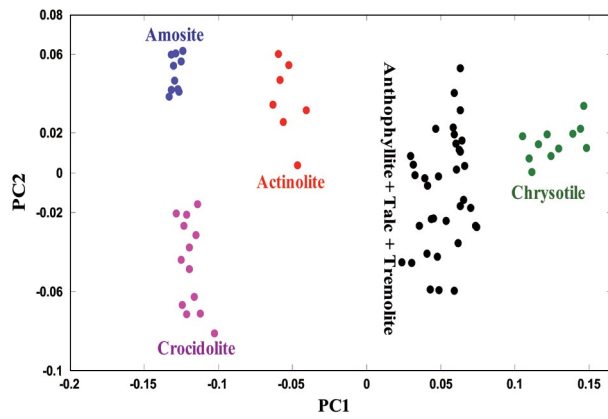


Fig. 3. PC scatter plot of six standard asbestos and talc (non-asbestos) samples on PC1 and PC2 for data obtained from low-Z particle EPMA.

mineral particles except anthophyllite and talc.

Anthophyllite ($(\text{Mg,Fe})_7\text{Si}_8\text{O}_{22}(\text{OH})_2$) is a mineral which is generated from the metamorphic reaction of talc ($\text{Mg}_3(\text{Si}_4\text{O}_{10})(\text{OH})_2$) and has similar chemical compositions with talc, except Fe in anthophyllite. The stoichiometric ratios of Mg/Si in anthophyllite and talc are 0.87 and 0.75 respectively, which are somewhat too close to be distinguished based on the EPMA data, i.e., the Mg/Si ratios are overlapping in the EPMA data as shown in the right panel of Fig. 2 (Mg/Si = 0.701–1.031 and 0.608–0.808 for anthophyllite and talc, respectively). When the EPMA X-ray data of anthophyllite were carefully examined, among analyzed 21 standard anthophyllite particles, 20 particles were identified in the pure form of anthophyllite, where 11 and 9 particles were with and without Fe, respectively. The remaining one particle turned out to be Mg-vermiculite as an impurity. The X-ray spectral data can be useful to distinguish between Fe-containing anthophyllite and talc particles, but it is difficult to clearly differentiate non-Fe-containing anthophyllite particles from talc.

3.2 ATR-FTIR Imaging

ATR-FTIR imaging technique was employed to distinguish between anthophyllite and talc. Fig. 4 shows secondary electron images (SEIs) before and after ATR-FTIR measurements, (C) ATR-FTIR PCA image, and (D) light optical image of anthophyllite particles on Ag foil. The same particles in the four images are denoted by particle number.

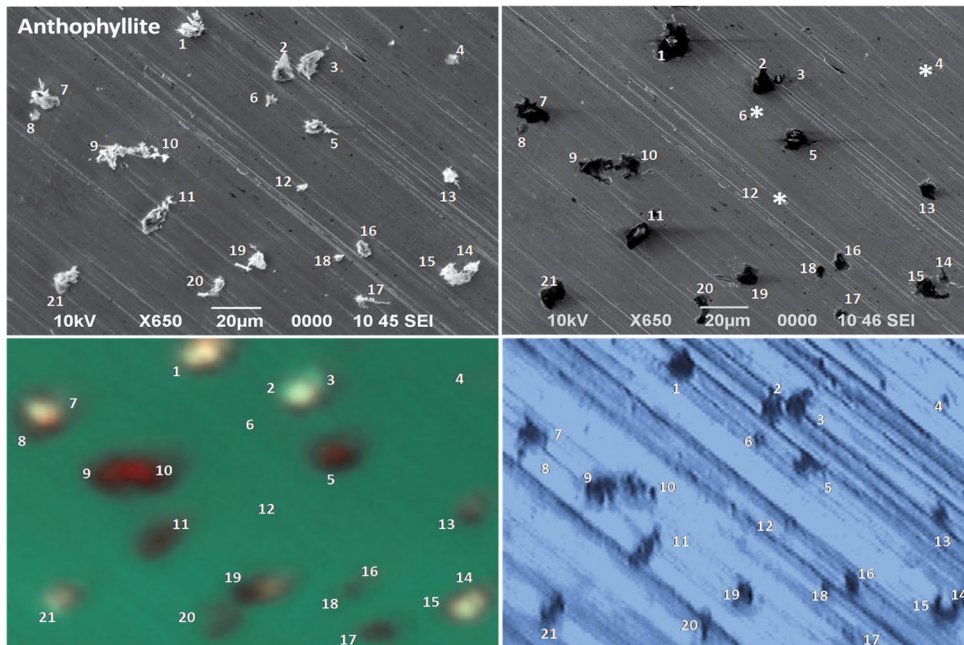


Fig. 4. Secondary electron images (SEIs) (A) before and (B) after ATR-FTIR measurements, (C) ATR-FTIR PCA image, and (D) light optical image of anthophyllite particles on Ag foil. The same particles in the four images are denoted by particle number.

FTIR measurements, ATR-FTIR PCA image, and light optical image of the same 21 individual anthophyllite particles on Ag foil. The ATR-FTIR image of Fig. 4C was obtained by the application of principle component analysis (PCA) after the first differentiation of original ATR-FTIR spectra at all the pixels in the image. Fig. 4D is a light optical image obtained from an optical microscope in the ATR-FTIR imaging instrument, which is used for the location of particles of interest. Although the quality of SEIs and ATR-FTIR images differs due to the inherently different spatial resolutions of the images (e.g., ~ 100 nm for the SEI and $3.9 \mu\text{m}$ at $1,000\text{--}1,200 \text{ cm}^{-1}$ for the ATR-FTIR image), the same patterns of particle location among the images ensure that the same particles of micrometer size were dealt with. Their equivalent diameters range from 1.54 to $6.12 \mu\text{m}$ (determined from SEI before ATR-FTIR measurement), where the equivalent diameter is calculated by assuming that a particle with the same area for a particle on SEI is circular. The area of each image is approximately $150 \times 110 \mu\text{m}^2$. Considering that the pixel size of an ATR-FTIR image is $1.56 \times 1.56 \mu\text{m}^2$, the number of pixels for the ATR-FTIR image is $\sim 6,780$. All pixels in the image contain full IR spectra ranging from $4,000$ to 680 cm^{-1} . Although the experimental ATR-FTIR imaging data were obtained on $1.56 \times 1.56 \mu\text{m}^2$ pixel size, the manufacture's software interpolates ATR-FTIR imaging pixel data onto a display image with many more pixels such that the final display image looks better than the actual image.

The SEIs clearly shows the morphology and locations of the 21 particles before and after ATR-FTIR imaging measurement. For the ATR-FTIR imaging measurement, the sample has to be in contact with the IRE crystal so that some force is applied to the sample during the contact. When they are in good contact and well pressed with the IRE crystal, particles are (partly or fully) embedded into the ductile Ag collecting foil. The nonconductive particles sitting on Ag foil (Fig. 4A) look bright because of high secondary and backscattered electron yields of insulating particles, whereas the particles on SEI taken after FTIR measurement look dark (Fig. 4B), as electrons can flow from the embedded particles into the metallic foil, resulting in low secondary and backscattered electron yields (Goldstein *et al.*, 2003). By comparing Fig. 4A and 4B, most particles spread out and some particles were reoriented and/or broken off into small parts as the force by the IRE crystal was applied on the particles. Some particles were missed during ATR-FTIR

imaging measurement (e.g., three particles with asterisk notation in Fig. 4B). This sort of modification made during ATR-FTIR measurements can be easily identified by comparing two SEIs collected before and after ATR-FTIR imaging measurements. As the locations and sizes of all the particles in the image field are known from the SEIs, their ATR-FTIR spectra can be extracted easily from raw ATR-FTIR image data.

The same type of low-Z particle EPMA and ATR-FTIR imaging experiments was carried out for the standard talc and tremolite samples, where 8 and 16 particles were analyzed, respectively. The most significant region of typical ATR-FTIR spectra (ranging from 700 cm^{-1} to $1,200 \text{ cm}^{-1}$) for single particles of tremolite, anthophyllite, and talc is shown in Fig. 5, where spectra for standard bulk samples are also shown as an inset. In case of tremolite, the spectral pattern with various significant differences in peak positions is sufficient to distinguish from individual anthophyllite and talc particles. The pattern of the ATR-FTIR spectra obtained from ATR-FTIR imaging measurement are somewhat similar both for the individual particles of anthophyllite and talc (Fig. 5). A very sharp and intense peak for Si-O stretching vibration is observed almost in the similar region, i.e., $1,008\text{--}1,012 \text{ cm}^{-1}$, for the individual particles of anthophyllite and talc. However, some significant differences are present in the ATR-FTIR spectra of anthophyllite and talc minerals, i.e., a weak Si-O stretching peak observed at $\sim 1,088 \text{ cm}^{-1}$ and $\sim 1,056 \text{ cm}^{-1}$ region for anthophyllite and talc,

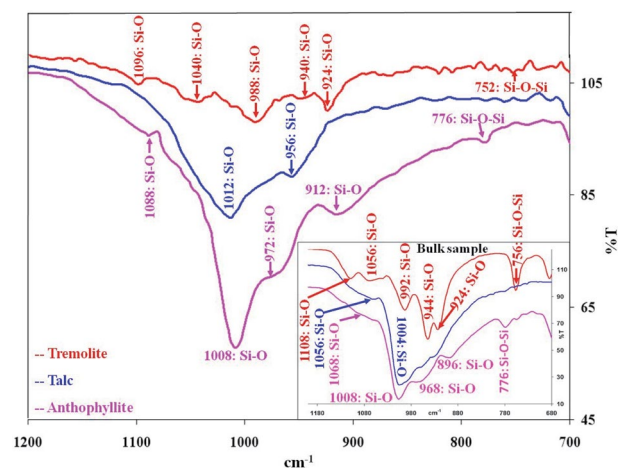


Fig. 5. Typical ATR-FTIR spectra of individual tremolite, anthophyllite, and talc particles. Spectra for the bulk sample of each mineral are shown as an inset. Data are shown only for the most significant spectral region of $700\text{--}1,200 \text{ cm}^{-1}$.

respectively. An additional ATR-FTIR peak at $\sim 912\text{ cm}^{-1}$ region is for anthophyllite, which is absent in talc. For anthophyllite, an ATR-FTIR peak at $\sim 776\text{ cm}^{-1}$ in the silicate chain stretching vibration region is observed, which is absent in talc, indicating that individual anthophyllite and talc particles of micrometer size can be differentiated from each other based on their ATR-FTIR spectra. On the other hand, this ATR-FTIR technique fails to provide the information on morphology and elemental compositions of mineral particles, which is also necessary for detailed mineral characterization. Therefore, the combined use of EPMA and ATR-FTIR data can be used to clearly distinguish between regulated asbestiform minerals and talc on a single particle basis, which is not somewhat sufficiently carried out by employing either technique individually.

4. CONCLUSIONS

In this work, it is shown that different asbestos minerals and talc can be unambiguously identified and distinguished from each other on a single particle basis by the combined use of low-Z particle EPMA and ATR-FTIR imaging techniques. Low-Z particle EPMA technique can distinguish between all the standard six asbestos mineral particles based on their chemical compositions, but it is not sufficient to differentiate non-Fe-containing anthophyllite asbestos from non-asbestiform talc. The ATR-FTIR imaging technique can clearly distinguish between anthophyllite and talc based on their different characteristic vibrational signals generated from the silicate structures. The combined application of these two different single particle analytical techniques can be useful for the characterization of individual asbestos and non-asbestos fiber particles than the techniques employed individually. Further works are required to substantiate the feasibility of this novel approach for the analysis of ambient asbestos and talc particles in the air.

ACKNOWLEDGEMENT

This study was supported by the National Research Foundation of Korea (NRF) grant funded by the Korean government (MSIT) (No. 2021R1A4A1032579 and No. 2021R1A2C2004240) and by the National Institute of Environmental Research (NIER) funded by the Ministry

of Environment (MOE) of Korea (NIER-2021-03-03-007).

REFERENCES

- Bernarde, M.A. (1990) *Asbestos: The Hazardous Fiber*. CRC Press, Boca Raton, USA.
- Bignon, J., Peto, J., Saracci, R. (1989) *Non-occupational Exposure to Mineral Fibres*, IARC Scientific Publication No. 90, International Agency for Research on Cancer, Lyon, France.
- Crabbe, J.V. (1966) Quantitative determination of chrysotile, amosite and crocidolite by x-ray diffraction. *American Industrial Hygiene Association Journal*, 27, 293–298.
- Crane, N.J., Bartick, E.G., Perlman, R.S., Huffman, S.J. (2007) Infrared spectroscopic imaging for noninvasive detection of latent fingerprints. *Journal of Forensic Science*, 52, 48–53. <https://doi.org/10.1111/j.1556-4029.2006.00330.x>
- Dodson, R.F., Atkinson, M.A.L. (2006) Measurements of asbestos burden in tissues. *Annals of the New York Academy of Sciences*, 1076, 281–291. <https://doi.org/10.1196/annals.1371.015>
- Dodson, R.F., Hammar, S.P., Poye, L.W. (2008) A Technical Comparison of Evaluating Asbestos Concentration by Phase-Contrast Microscopy (PCM), Scanning Electron Microscopy (SEM), and Analytical Transmission Electron Microscopy (ATEM) as Illustrated From Data Generated From a Case Report. *Inhalation Toxicology*, 20, 723–732. <https://doi.org/10.1080/08958370701883250>
- Dodson, R.F., Hammer, S.P. (2011) *Asbestos: Risk Assessment, Epidemiology, and Health Effects*. CRC Press, Taylor and Francis Group, Boca Raton, USA.
- Gardner, M.J., Powell, C.A. (1986) Mortality of asbestos cement workers using almost exclusively chrysotile fibre. *Journal of the Society of Occupational Medicine*, 36, 124–126.
- Goldstein, J.I., Newbury, D.E., Joy, D.C., Lyman, C., Echlin, P., Lifshin, E., Sawyer, L., Michael, J. (2003) *Scanning Electron Microscopy and X-ray Microanalysis*. (3rd Ed.), Kluwer-Plenum, New York, USA.
- Goodhead, K., Martindale, R.W. (1969) The determination of amosite and chrysotile in airborne dusts by an X-ray diffraction method. *Analyst*, 94, 985–988.
- Griffiths, P.R., de Haseth, J.A. (2007) *Fourier Transform Infrared Spectrometry*. (2nd Ed.), John Wiley & Sons, Inc., Hoboken, NJ, USA.
- Hodgson, A.A. (1986) *Scientific Advances in Asbestos, 1967 to 1985*. Anjalena Publication, Crowthorne, UK.
- Jackson, J.E. (1991) *A User's Guide to Principal Components*. John Wiley and Sons, Hoboken, NJ, USA.
- Janik, H., Wrona, M. (2019) Asbestos. In *Encyclopedia of Analytical Science* (Worsfold, P., Townshend, A., Poole, C. Eds), Elsevier, Oxford, UK, pp. 107–116.
- Jolliffe, I.T., Cadima, J. (2016) Principal component analysis: a review and recent developments. *Philosophical Transactions of the Royal Society A*, 374, 20150202. <https://doi.org/10.1098/rsta.2015.0202>

- 1098/rsta.2015.0202
- Jung, H.J., Malek, M.A., Ryu, J.Y., Kim, B.W., Kim, H., Ro, C.-U. (2010) Speciation of Individual Mineral Particles of Micrometer Size by the Combined Use of Attenuated Total Reflectance-Fourier Transform-Infrared Imaging and Quantitative Energy-Dispersive Electron Probe X-ray Microanalysis Techniques. *Analytical Chemistry*, 82(14), 6193–6202. <https://doi.org/10.1021/ac101006h>
- Jung, H.J., Eom, H.J., Kang, H.W., Moreau, M., Sobanska, M., Ro, C.-U. (2014) Combined use of quantitative ED-EPMA, Raman microspectrometry, and ATR-FTIR imaging techniques for the analysis of individual particles. *Analyst*, 139(16), 3949–3960. <https://doi.org/10.1039/C4AN00380B>
- Keane, M.J., Wallace, W.E. (1995) Pulmonary surfactant adsorption and the expression of silica toxicity. In *Silica and Silica-induced Lung Diseases* (Castranova, V., Vallyathan, V., Wallace, W.E. Eds), CRC Press, Boca Raton, USA, pp. 271–281.
- Khan, M.S.I., Hwang, H., Kim, H., Ro, C.-U. (2008) Molecular mass concentrations for a powdered SRM sample using a quantitative single particle analysis. *Analytica Chimica Acta*, 619(1), 14–19. <https://doi.org/10.1016/j.aca.2008.03.020>
- Knox, J.F., Holmes, S., Doll, R., Hill, D. (1968) Mortality from lung cancer and other causes among workers in an asbestos textile factory. *Occupational and Environmental Medicine*, 25, 293–303.
- Langer, A.M., Rubin, I.B., Selikoff, I.J. (1972) Chemical characterization of asbestos body cores by electron microprobe analysis. *Journal of Histochemistry and Cytochemistry*, 20, 723–734.
- Lee, K.P., Abraham, J.L. (1985) Lung Response to Particulates with Emphasis on Asbestos and other Fibrous Dusts. *Critical Reviews in Toxicology*, 14, 33–86. <https://doi.org/10.3109/10408448509023764>
- Malek, M.A., Kim, B.W., Jung, H.J., Song, Y.C., Ro, C.-U. (2011) Single-Particle Mineralogy of Chinese Soil Particles by the Combined Use of Low-Z Particle Electron Probe X-ray Microanalysis and Attenuated Total Reflectance-FT-IR Imaging Techniques. *Analytical Chemistry*, 83, 7970–7977. <https://doi.org/10.1021/ac201956h>
- Malek, M.A., Eom, H.J., Hwang, H., Hur, S.D., Hong, S., Hou, S., Ro, C.-U. (2019) Single particle mineralogy of microparticles from Himalayan ice-cores using SEM/EDX and ATR-FTIR imaging techniques for identification of volcanic ash signatures. *Chemical Geology*, 504, 205–215. <https://doi.org/10.1016/j.chemgeo.2018.11.010>
- Michaels, L., Chissick, S.S. (1981) *Asbestos: Properties, Applications and Hazards*. John Wiley and Sons, Toronto, Canada.
- Millette, J.R. (2006) Asbestos analysis methods. In *Asbestos: Risk assessment, epidemiology, and health effects* (Dodson, R.F. and Hammar, S.P. Eds), Taylor & Francis, Boca Raton, USA, pp. 9–38.
- Murray, R. (1990) Asbestos: a chronology of its origins and health effects. *British Journal of Industrial Medicine*, 47(6), 361–365. <https://doi.org/10.1136/oem.47.6.361>
- Newhouse, M.L., Thomson, H. (1965) Mesothelioma of pleura and peritoneum following exposure to asbestos in the London area. *British Journal of Industrial Medicine*, 22, 261–269.
- Rickards, A.L. (1972) Estimation of trace amounts of chrysotile asbestos by x-ray diffraction. *Analytical Chemistry*, 44, 1872–1873. <https://doi.org/10.1021/ac60319a050>
- Ro, C.-U., Osan, J., Van Grieken, R. (1999) Determination of Low-Z Elements in Individual Environmental Particles Using Windowless EPMA. *Analytical Chemistry*, 71, 1521–1528. <https://doi.org/10.1021/ac981070f>
- Ro, C.-U., Osan, J., Szaloki, I., Oh, K.Y., Kim, H., Van Grieken, R. (2000) Determination of chemical species in individual aerosol particles using ultrathin window EPMA. *Environmental Science and Technology*, 34(14), 3023–3030. <https://doi.org/10.1021/es9910661>
- Ro, C.-U., Oh, K.Y., Kim, H., Kim, Y.P., Lee, C.B., Kim, K.H., Kang, C.H., Osan, J., de Hoog, J., Worobiec, A., Van Grieken, R. (2001) Single-Particle Analysis of Aerosols at Cheju Island, Korea, Using Low-Z Electron Probe X-ray Microanalysis: A Direct Proof of Nitrate Formation from Sea Salts. *Environmental Science and Technology*, 35(22), 4487–4494. <https://doi.org/10.1021/es0155231>
- Ro, C.-U., Osan, J., Szaloki, I., de Hoog, J., Worobiec, A., Van Grieken, R. (2003) A Monte Carlo program for quantitative electron-induced X-ray analysis of individual particles. *Analytical Chemistry*, 75, 851–859. <https://doi.org/10.1021/ac025973r>
- Rohl, A.N., Langer, A.M. (1974) Identification and quantitation of asbestos in talc. *Environ Health Perspect*, 9, 95–109. <https://doi.org/10.1289/ehp.74995>
- Selikoff, I.J., Churg, J., Hammond, E.C. (1964) Asbestos exposure and neoplasia. *Journal of the American Medical Association*, 188, 22–26. <https://doi.org/10.1001/jama.1964.03060270028006>
- Skinner, H.C.W., Ross, M., Frondel, C. (1988) *Asbestos and Other Fibrous Materials*. Oxford Press, New York, USA.
- Song, Y.C., Eom, H.J., Jung, H.J., Malek, M.A., Kim, H., Geng, H., Ro, C.-U. (2013) Investigation of aged Asian dust particles by the combined use of quantitative ED-EPMA and ATR-FTIR imaging. *Atmospheric Chemistry and Physics*, 13(6), 3463–3480. <https://doi.org/10.5194/acp-13-3463-2013>
- Sporn, T.A., Roggli, V.L. (2004) Mesothelioma. In *Pathology of Asbestos-Associated Diseases*, 2nd Edition (Oury, T.D., Sporn, T.A., Roggli, V.L. Eds), Springer, Berlin, Germany.
- Van Dalen, G., Heussen, P.C.M., Den Adel, R., Hoeve, R.B. (2007) Attenuated Total Internal Reflection Infrared Microscopy of Multilayer Plastic Packaging Foils. *Journal of Applied Spectroscopy*, 61, 593–602. <https://doi.org/10.1366/000370207781269738>
- Vekemans, B., Janssens, K., Vincze, L., Adams, F., Van Espen, P. (1994) Analysis of X-ray spectra by iterative least squares (AXIL): New developments. *X-Ray Spectrometry*, 23, 278–285.
- WHO (World Health Organization) (1986) *Asbestos and Other Natural Mineral Fibers*. Geneva, Switzerland. <https://apps.who.int/iris/handle/10665/37190>
- Wright, G.D. (1969) Asbestos and health in 1969. *American Review of Respiratory Disease*, 100, 467–479.